Inorganic Chemistry

Article

pubs.acs.org/IC

Peri-Substituted (Ace)Naphthylphosphinoboranes. (Frustrated) Lewis Pairs

Jens Beckmann,*[,†] Emanuel Hupf,[†] Enno Lork,[†] and Stefan Mebs*[,‡]

[†]Institut für Anorganische Chemie, Universität Bremen, Leobener Straße, 28359 Bremen, Germany

[‡]Institut für Chemie und Biochemie, Freie Universität Berlin, Fabeckstraße 36a, 14195 Berlin, Germany

Supporting Information

ABSTRACT: The synthesis and molecular structures of 1-(diphenylphosphino)-8-naphthyldimesitylborane (**1**) and 5-(diphenylphosphino)-6-acenaphthyldimesitylborane (**2**) are reported. The experimentally determined P−B *peri* distances of 2.162(2) and 3.050(3) Å allow **1** and **2** to be classified as regular and frustrated Lewis pairs. The electronic characteristics of the (non)bonding P−B contacts are determined by analysis of a set of real-space bonding indicators (RSBIs) derived from the theoretically calculated electron and pair densities. These densities are analyzed utilizing the atoms-in-molecules (AIM), stockholder, and electron-localizability-indicator (ELI-D) space partitioning schemes. The recently introduced mapping of the electron localizability on the ELI-D basin surfaces is also applied. All RSBIs clearly discriminate the bonding P−B contact in **1** from the nonbonding P−B contact in **2**, which is due to the fact that the acenaphthene framework is rather rigid, whereas the naphthyl framework shows sufficient conformational flexibility, allowing shorter *peri* interations. The results are compared to the previously known prototypical phosphinoborane $Ph_3PB(C_6F_5)_3$, which serves as a reference for a bonding P−B interaction. The most prominent features of the nonbonding P−B contact in **2** are the lack of an AIM bond critical point, the unaffected Hirshfeld surfaces of the P and B atomic fragments, and the negligible penetration of the electron population of the ELI-D lone pair basin of the P atom into the AIM B atomic basin.

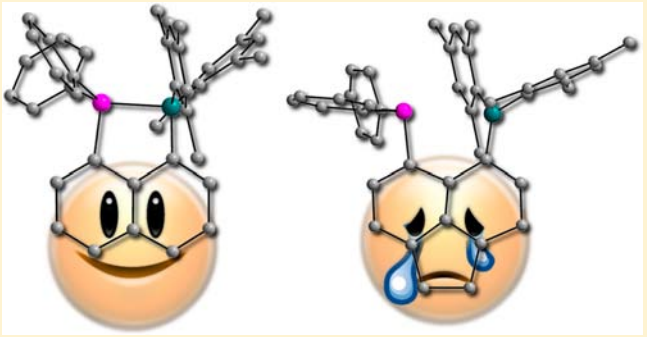

INTRODUCTION

The discovery of frustrated Lewis pairs (FLPs) and their potential for the metal-free activation of small molecules, such as dihydrogen and carbon dioxide, marks a paradigm change in the field of catalysis.[1−3] One of the first FLP examples involves the FLP perfluorotriphenylborane $B(C_6F_5)_3$/1,8-bis-(diphenylphosphinonaphthalene) 1,8-$(Ph_2P)_2$-Nap (**I**), which activates dihydrogen for the catalytic hydrogenation of silyl enol ethers (Scheme 1).[4] Another relevant example includes the FLP 1,8-bis(perfluorodiphenylboryl)naphthalene 1,8-$[(C_6F_5)_2B]_2$-Nap (**II**)/2,2,6,6-tetramethylpiperidine, which has been used for catalytic hydrogenation of imines.[5] The utility of **I** and **II** for these catalytic reactions prompted us to investigate whether both Lewis acid and Lewis base containing the elements P/B can be incorporated into the *peri* positions of the same naphthalene and acenaphthene structures to give rise to intramolecular FLPs. We therefore engaged in the preparation and structural elucidation of 1-(diphenylphosphino)-8-naphthyldimesitylborane, 1-(Ph_2P)-8-(Mes_2B)-Nap (**1**), and the related 5-(diphenylphosphino)-6-acenaphthyldimesitylborane, 5-(Ph_2P)-6-(Mes_2B)-Ace (**2**), possessing the same substituents at the P and B atoms but quite different P−B *peri* distances of 2.162(2) and 3.050(3) Å, thus comprising straightforward examples of regular Lewis pairs and FLPs (Scheme 1). During the course of our work, three related studies of phoshinonaphthylboranes became available: An experimental and theoretical study of **1** and the frustrated (open) form of **1** was reported by Wang et al.[6]

Scheme 1. 1,8- and 5,6-Disubstituted Naphthalenes and Acenaphthenes and P−B *Peri* Distances

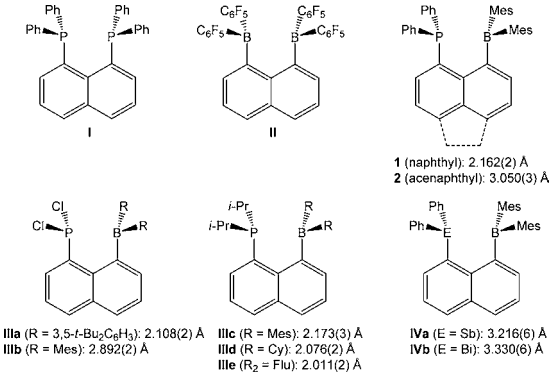

Received: June 6, 2013
Published: September 30, 2013

Two 1-(dichlorophosphino)-8-naphthyldiarylboranes, 1-(Cl_2P)-8-(R_2B)-Nap (**IIIa**, R = 3,5-*t*-$Bu_2C_6H_3$; **IIIb**, R = Mes), were published by Tokitoh et al.[7] and structural data disclosed during a conference presentation.[8] Three 1-(diisopropylphosphino)-8-naphthyldiorganoboranes, 1-(*i*-Pr_2P)-8-(R_2B)-Nap (**IIIc**, R = Mes; **IIId**, R = Cy; **IIIe**, R_2 = Flu), were prepared by Bourissou et al.[9] The different P−B *peri* distances of 2.108(2) (**IIIa**), 2.892(2) (**IIIb**), 2.173(3) (**IIIc**), 2.076(2) (**IIId**), and 2.011(2) (**IIIe**) Å confirm that the substituents of the P and B atoms can provide fine-tuning covering a large range of different bonding situations. It is also noteworthy that **1** is a lighter congener of 1-(diphenylstilbino)-8-naphthyldimesitylborane, 1-(Ph_2Sb)-8-(Mes_2B)-Nap (**IVa**), and 1-(diphenylbismutio)-8-naphthyldimesitylborane, 1-(Ph_2Bi)-8-(Mes_2B)-Nap (**IVb**), possessing Sb−B and Bi−B *peri* distances of 3.216(6) and 3.330(6) Å, respectively (Scheme 1).[10]

The aforementioned examples suggest that the two atoms in the *peri* positions can be assorted by attractive and repulsive forces to various degrees. The focus of the present study is the influence of the naphthyl and acenaphthyl moieties to the P−B interaction, which, to the best of our knowledge, has not been investigated before.

So far, the bond situation in related naphthalenes and acenaphthenes has been almost entirely analyzed by inspection of the molecular geometries, which may not lead to an unambiguous distinction between bonding and nonbonding *peri* interactions. Only a few studies have also utilized additional natural bond orbital (NBO) analysis[6,9−15] and/or topological analysis of the electron density (ED) according to the atoms-in-molecules (AIM) theory.[6,9,15−17] The space-filling AIM approach has found wide applications in chemistry as a complement for molecular orbital (MO) calculations as well as exclusive interpretation of the geometrical parameters, because it provides consistent atomic as well as bonding properties.[18] Unlike MO and NBO, the ED can, in principle, be obtained from theoretical calculations as well as from high-resolution X-ray diffraction data. In this work, we combine theoretical AIM analyses with the stockholder[19] and electron-localizability-indicator (ELI-D)[20] space-partitioning schemes. The stockholder partitioning is used for generation of the Hirshfeld surfaces,[21] which can be applied to any fragment (atoms, functional groups, molecules, etc.) in order to uncover contact patches between the fragments. The ELI-D divides space into regions of localized electron pairs instead of atoms and therefore eminently complements the AIM theory. For the interpretation of atom−atom interactions, the concept of ELI-D valence basins overlapping with AIM atoms is very helpful.[22] It quantifies the partial electron numbers of a ELI-D bonding basin within the bond contributing AIM atoms. It was developed by Raub and Jansen based on the electron localization function and used primarily for estimation of the bond polarities. The Raub−Jansen index (RJI) is 50% for homopolar bonds and increases for polar interactions.

In an extensive analysis of the N−B bonds of small Lewis acid−base adducts as well as *arachno*-boranes, it was revealed that dative bonds are represented by an RJI of at least 95%.[23]

With this pooling of real-space bonding indicators (RSBIs), the P−B bonding in **1** can unambiguously be discriminated from the nonbonding P−B contact in **2**. The Lewis complex $Ph_3PB(C_6F_5)_3$ serves as a prototypical reference compound with a bonding P−B interaction.[24]

EXPERIMENTAL SECTION

General Procedures. Reagents were obtained commercially (Sigma-Aldrich, Germany) and were used as received. Dry solvents were collected from an mBraun SPS800 solvent system. The starting materials 1-bromo-8-(diphenylphosphino)naphthalene, 5-bromo-6-(diphenylphosphino)acenaphthene,[25] and dimesitylfluoroborane[26] were prepared according to literature procedures. ^{1}H, ^{11}B, ^{13}C, and ^{31}P NMR spectra were recorded in $CDCl_3$ at room temperature using a Bruker Avance-360 spectrometer and are referenced to tetramethylsilane (^{1}H, ^{13}C), boron trifluoride diethyl etherate (^{11}B), and phosphoric acid (85% in water; ^{31}P). Chemical shifts are reported in parts per million (ppm), and coupling constants (*J*) are given in Hertz (Hz). High-resolution electron-impact mass spectrometry (HREIMS) spectra were collected using a Finnigan MAT 95 spectrometer and referenced to the isotopomers containing ^{10}B. Microanalyses were carried out by Analytische Laboratorien GmbH (Lindlar, Germany).

Synthesis of 1-(Diphenylphosphino)-8-naphthyldimesitylborane, 1-(Ph_2P)-8-($BMes_2$)-Nap (1). *n*-Butyllithium (1.28 mmol, 2.5 M in *n*-hexane) and *N*,*N*,*N*′,*N*′-tetramethylethylenediamine (150 mg, 1.28 mmol) were added to a suspension of 1-bromo-8-(diphenylphosphino)naphthalene (250 mg, 0.64 mmol) in diethyl ether (3 mL) and stirred for 2 h at −78 °C. The suspension was allowed to warm to room temperature, and a solution of dimesitylfluoroborane (340 mg, 1.28 mmol) in diethyl ether (2 mL) was added dropwise and stirred for 12 h. After aqueous workup, removal of the solvent by rotary evaporation afforded a crude product (yield >95% by ^{31}P NMR), which was recrystallized three times from dichloromethane/*n*-hexane to obtain **1** as yellow single crystals (130 mg, 0.23 mmol, 37%; mp 213 °C).

^{1}H NMR: δ 8.16 (d, J = 8 Hz, 1H), 7.80 (m, 4H), 7.65 (m, 1H), 7.51 (m, 5H), 7.15 (t, J = 7 Hz, 1H), 6.90 (m, 2H), 6.84 (s, 1H), 6.65 (m, 3H), 6.42 (s, 1H), 6.08 (s, 1H), 2.34 (s, 3H, CH_3), 2.13 (s, 3H, CH_3), 2.04 (s, 3H, CH_3), 1.99 (s, 3H, CH_3), 1.31 (s, 3H, CH_3), 1.28 (s, 3H, CH_3). ^{13}C{^{1}H} NMR: δ 156.4 (d, $J(^{31}P-^{13}C)$ = 17 Hz), 143.8, 143.7, 143.6, 143.4, 142.8, 142.7 (d, $J(^{31}P-^{13}C)$ = 8 Hz), 142.4, 141.5 (d, $J(^{31}P-^{13}C)$ = 11 Hz), 135.1 (d, $J(^{31}P-^{13}C)$ = 11 Hz), 133.2, 133.1, 132.9, 132.4 (d, $J(^{31}P-^{13}C)$ = 7 Hz), 131.7 (d, $J(^{31}P-^{13}C)$ = 46 Hz), 131.7, 130.7 (d, $J(^{31}P-^{13}C)$ = 46 Hz), 129.4 (d, $J(^{31}P-^{13}C)$ = 71 Hz), 128.7 (d, $J(^{31}P-^{13}C)$ = 17 Hz), 128.6, 128.4, 128.2, 126.5 (d, $J(^{31}P-^{13}C)$ = 9 Hz), 125.3 (d, $J(^{31}P-^{13}C)$ = 6 Hz), 124.6 (d, $J(^{31}P-^{13}C)$ = 2 Hz), 26.1 (s, CH_3), 26.0 (s, CH_3), 25.7 (s, CH_3), 24.7 (s, CH_3), 20.9 (s, CH_3), 20.5 (s, CH_3). ^{11}B{^{1}H} NMR: δ 16.2 (br). ^{31}P{^{1}H} NMR: δ 12.2. HREIMS. Calcd for $C_{40}H_{38}{}^{10}BP$: 559.28405. Found: 559.28211. Anal. Calcd for $C_{40}H_{38}BP$: C, 85.71; H, 6.83. Found: C, 85.20; H, 6.93.

Synthesis of 5-(Diphenylphosphino)-6-acenaphthyldimesitylborane, 5-(Ph_2P)-6-($BMes_2$)-Ace (2). To a suspension of 5-bromo-6-(diphenylphosphino)acenaphthene (250 mg, 0.60 mmol) in diethyl ether (5 mL) at −78 °C were added dropwise *n*-butyllithium (1.20 mmol, 2.5 M in *n*-hexane) and *N*,*N*,*N*′,*N*′-tetramethylethylenediamine (140 mg, 1.20 mmol). After 2 h, the reaction mixture was allowed to warm to room temperature, and a solution of dimesitylfluoroborane (320 mg, 1.20 mmol) in diethyl ether (2 mL) was added. Stirring was continued for a further 12 h. After aqueous workup, the solvent was removed by rotary evaporation. The crude product (yield >95% by ^{31}P NMR) was recrystallized from dichloromethane/*n*-hexane, affording **2** as colorless crystals (240 mg, 0.41 mmol, 68%; mp >235 °C).

^{1}H NMR: δ 7.40 (m, 2H), 7.20 (m, 8H), 6.97 (t, J = 7 Hz, 2H), 6.85 (s, 1H), 6.77 (s, 1H), 6.73 (t, J = 7 Hz, 2H), 6.20 (s, 2H) 3.45 (m, 4H, H-1,2), 2.45 (s, 3H, CH_3), 2.32 (s, 3H, CH_3), 2.15 (s, 3H, CH_3), 1.95 (s, 3H, CH_3), 1.80 (s, 3H, CH_3), 1.02 (s, 3H, CH_3). ^{13}C{^{1}H} NMR: δ 149.3, 149.0 (d, $J(^{31}P-^{13}C)$ = 3 Hz), 146.0 (d, $J(^{31}P-^{13}C)$ = 8 Hz), 145.5, 143.5 (d, $J(^{31}P-^{13}C)$ = 6 Hz), 141.7, 141.4, 141.4, 141.0, 140.5, 140.3, 140.2 (d, $J(^{31}P-^{13}C)$ = 6 Hz), 139.1 (d, $J(^{31}P-^{13}C)$ = 9 Hz), 138.6 (d, $J(^{31}P-^{13}C)$ = 4 Hz), 138.1 (d, $J(^{31}P-^{13}C)$ = 3 Hz), 137.6, 135.0 (d, $J(^{31}P-^{13}C)$ = 5 Hz), 132.5 (d, $J(^{31}P-^{13}C)$ = 17 Hz), 132.0 (d, $J(^{31}P-^{13}C)$ = 14 Hz), 129.8 (d, $J(^{31}P-^{13}C)$ = 3 Hz), 129.2 (d, $J(^{31}P-^{13}C)$ = 6 Hz), 128.5 (d,

dx.doi.org/10.1021/ic401406k | Inorg. Chem. 2013, 52, 11881−11888

$J(^{31}P-^{13}C)$ = 2 Hz), 128.5, 128.2, 128.1, 128.0, 127.9, 127.8, 127.2, 127.1, 120.1 (d, $J(^{31}P-^{13}C)$ = 1 Hz), 119.9, 30.5 (s, CH_2), 30.3 (s, CH_2), 25.2 (s, CH_3), 25.0 (s, CH_3), 24.5 (CH_3), 24.2 (CH_3), 23.4 (CH_3), 23.3 (CH_3), 21.2 (CH_3), 21.0 (CH_3). $^{31}P\{^1H\}$ NMR: δ −9.7. HREIMS. Calcd for $C_{42}H_{40}{}^{10}BP$: 585.29970. Found: 585.29563. Anal. Calcd for $C_{42}H_{40}BP$: C, 86.00; H, 6.87. Found: C, 85.15; H, 6.98.

X-ray Crystallography. Intensity data of **1** and **2** were collected on a Siemens P4 diffractometer fitted with graphite-monochromated Mo Kα (0.7107 Å) radiation. The structures were solved by direct methods and refined based on F^2 using *OLEX2*.[27] All non-H atoms were refined using anisotropic displacement parameters. H atoms attached to C atoms were included in geometrically calculated positions using a riding model. Disorder was resolved for **2** and refined with occupancy ratios of 51:49 (C30−C35), 52:48 (C1, C2, C13−C17, and C40−C48), and 59:41 (C20−C25). Crystal and refinement data are collected in Table S1 in the Supporting Information (SI). Crystallographic data (excluding structure factors) for structural analyses have been deposited with the Cambridge Crystallographic Data Centre as CCDC 941915 (**1**) and 941916 (**2**). Copies of this information may be obtained free of charge from The Director, CCDC, 12 Union Road, Cambridge CB2 1EZ, U.K. (fax +44-1223-336033, e-mail deposit@ccdc.cam.ac.uk, or http://www.ccdc.cam.ac.uk).

Computational Methodology. The experimentally obtained atomic coordinates of **1**, **2**, and $Ph_3PB(C_6F_5)_3$[24] were taken for a single-point calculation by applying the functional B3PW91[28] and the 6-311+G(2df,p)[29] basis set using the program package *Gaussian09*.[30] The C−H distances of all substances were set to neutron diffraction data prior to processing.[31] For AIM analyses, wave function files were generated along with single-point calculations and analyzed using *AIM2000*.[32] *DGrid* was used to analyze the ELI-D-related bond descriptors using a grid step size of 0.05 au.[33]

RESULTS AND DISCUSSION

The reaction of 1-bromo-8-(diphenylphosphino)naphthalene, 1-Br-8-(Ph_2P)-Nap, and 5-bromo-6-(diphenylphosphino)-acenaphthene, 5-Br-6-(Ph_2P)-Ace, with *n*-butyllithium (*n*-BuLi) in the presence of *N*,*N*,*N*′,*N*′-tetramethylethylendiamine at −78 °C proceeded with facile metal halide exchange and gave rise to formation of the corresponding lithium organyles. The subsequent salt metathesis reaction with dimesitylfluoroborane (Mes_2BF) at room temperature produced 1-(diphenylphosphino)-8-naphthyldimesitylborane, 1-(Ph_2P)-8-(Mes_2B)-Nap (**1**), and the related 5-(diphenylphosphino)-6-acenaphthyldimesitylborane, 5-(Ph_2P)-6-(Mes_2B)-Ace (**2**), after recrystallization in 37% and 68% yield (Scheme 2). Compounds **1** and **2** were obtained as high-melting yellow and colorless crystals that are readily soluble in most common organic solvents. Besides the color difference, the quite dissimilar ^{31}P NMR chemical shifts ($CDCl_3$) of **1** (δ 12.2) and **2** (δ −9.7) gave the first evidence that the bond situation might be different. The ^{11}B NMR spectrum ($CDCl_3$) of **1** shows a signal at δ 16.2, which is identical with that of **IIIc** and indicative of a tetracoordinated B atom. Surprisingly, no reasonable ^{11}B NMR spectrum ($CDCl_3$) was obtained for a concentrated solution of **2** in the temperature range between −60 and +20 °C. The molecular structures of **1** and **2** are shown in Figures 1 and 2. Selected interatomic distances and angles are collected in Table 1.

Scheme 2. Synthesis and ^{31}P NMR Chemical Shifts ($CDCl_3$) of 1 and 2

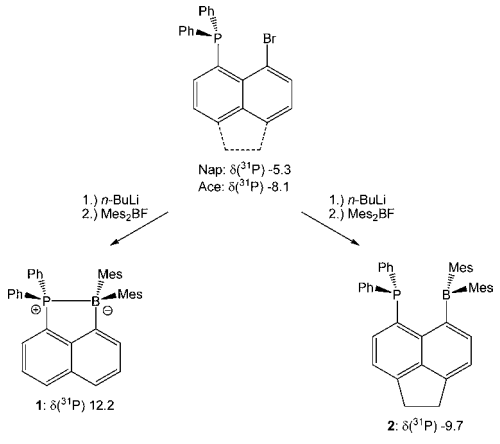

A comparison of both structures reveals strikingly different P−B distances of 2.162(2) and 3.050(3) Å, which unambiguously allows **1** and **2** to be classified as regular Lewis pairs and FLPs. Notably, the first value resembles the P−B distance of $Ph_3PB(C_6F_5)_3$ [2.180(6) Å].[24] The second value is by about 0.9 Å longer but significantly shorter than the sum of the van der Waals radii of the elements P/B (3.72 Å),[35] a commonly used, yet questionable upper limit for secondary interactions. All geometrical parameters of **1** resemble those recently published by Wang et al.[6] In **2**, the spatial arrangement of the B atom is almost planar, which is reflected in the sum of the C−B−C bond angles being close to 360° ($\sum_\alpha B$ = 358.4°) and a small distance of the B atom to the corresponding C_3 plane [$d_B(C_3)$ = 0.12 Å]. These values are close to those found for **IIIb** [d(PB) = 2.892(2) Å; $\sum_\alpha B$ = 359.0°],[8] in which the bulky substituents prevent a closer P−B contact. In **1**, a significant pyramidalization of the B atom is realized [$\sum_\alpha B$ = 346.6°; $d_B(C_3)$ = 0.35 Å], which is close to those of **IIIa** [d(PB) = 2.108(2) Å; $\sum_\alpha B$ = 348.1°][8] and **IIIc**−**IIIe**.[9] Despite the different spatial arrangements of the B atoms, the C40−B1−C50 angles of **1** [118.5(2) Å] and **2** [119.5(2) Å] vary only marginal. The spatial arrangement of the P atoms of **1** and **2** is distorted tetrahedral. The C20−P1−C30 angle of **1** [103.7(2)°] is smaller than the ideal tetrahedral angle, whereas that of **2** [113.2(4)°] is larger. It is noteworthy that only the P atom is significantly shifted toward the B atom upon P−B bond formation because the P1−C18−C19 angle [110.8(2)°] is much smaller than the B1−C10−C19 angle [119.2(2)°], although both the P and B atoms show considerable out-of-plane displacement [0.2753(5) and 0.268(3) Å]. The same trend was found in a structural study on related phosphinonaphthylboranes.[9] In **2**, the P and B atoms are also significantly displaced [0.173(1) and 0.369(3) Å], thus ruling out this parameter for discrimination between atom−atom attraction and repulsion. The ring distortion is very similar for both compounds. Usually, the small structural difference when going from the naphthalene to the acenaphthene frameworks accounts mainly for an elongation of the *peri* distance of about 0.2 Å.[14]

Figure 2a displays superposition of the molecular structures of **1** and **2**. When the P and B atoms are disregarded, the most obvious difference between both molecular structures is the orientation of the phenyl ring attached to the P atom, which is marked by a red arrow in the figure. In **1**, the corresponding phenyl ring plane is pointing between the ring planes of the two mesityl substituents, which allows one to accommodate a close proximity of the P and B atoms. In contrast, in **2**, this phenyl ring is oriented almost perpendicular to the phenyl ring in **1**; however, in solution, there is no evidence that this conformation is persistent. In fact, the orientation of the phenyl rings of **2** is of minor importance because the large P−B

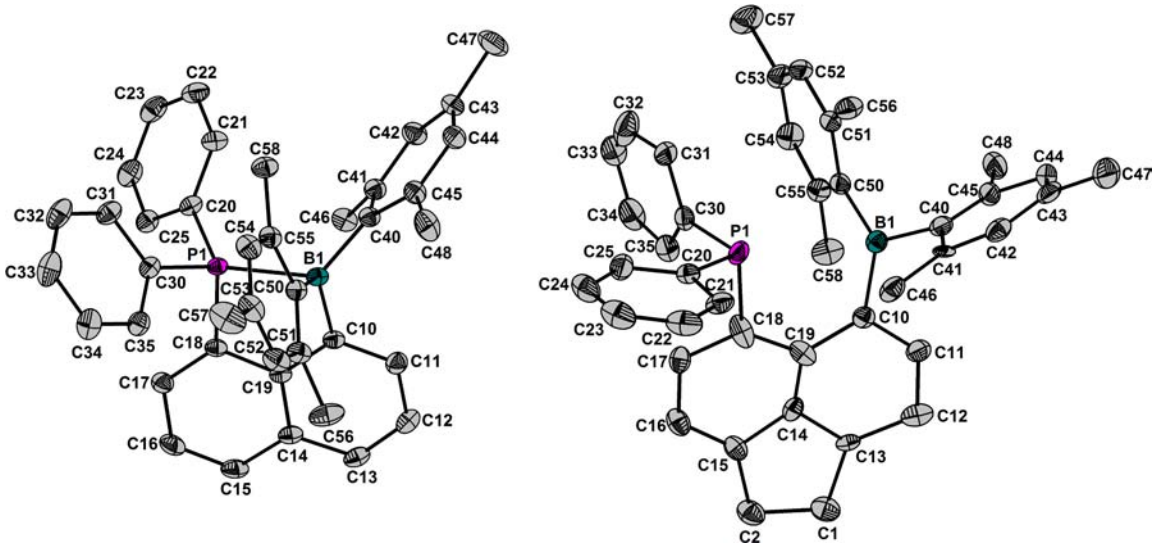

Figure 1. Molecular structures of **1** and **2** showing 30% probability ellipsoids and the crystallographic numbering scheme. *DIAMOND* presentation.[34]

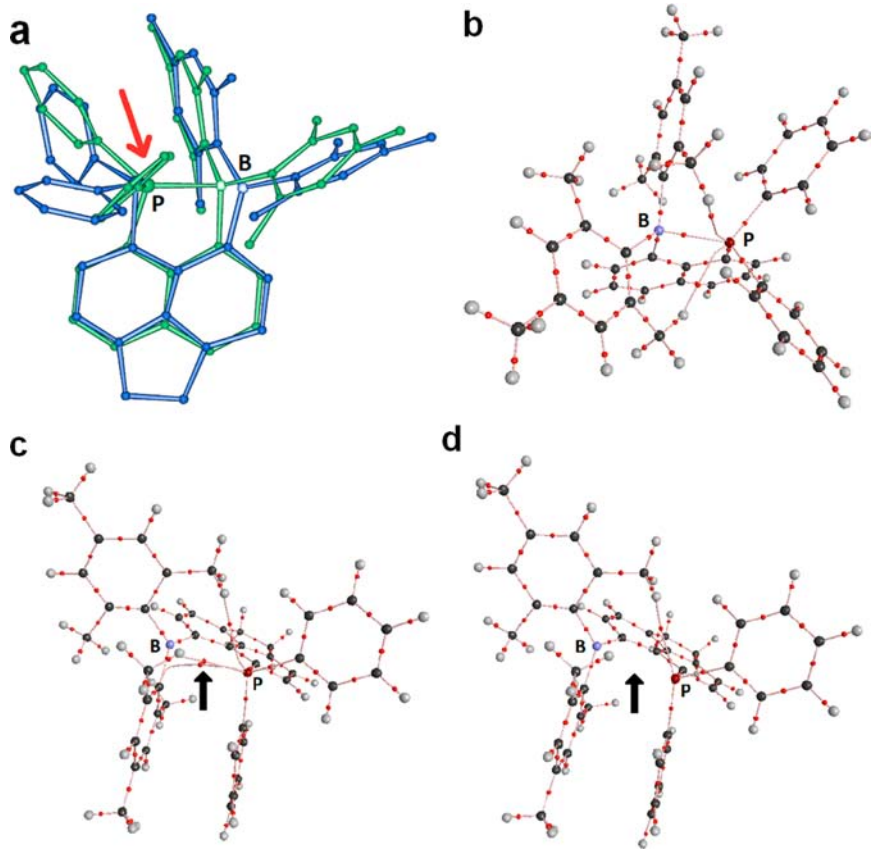

Figure 2. (a) Superposition of the experimental X-ray structures of **1** (green) and **2** (blue). *SCHAKAL* presentation.[36] (b) Bond topology of **1**. (c) Bond topology and (d) virial field of **2**. Red dots: bond critical points. For clarity, C−C, C−H, and H−H bond critical points as well as ring and cage critical points are not displayed. *AIM2000* presentation.[32]

distance is controlled by the rigidity of the acenaphthene framework. In turn, the naphthyl framework shows a higher conformational flexibility, allowing shorter *peri* interactions. This is reflected in all real-space bonding descriptors utilizing the AIM, Hirshfeld, and ELI-D space-partitioning schemes. The qualitative bond topology of the ED in terms of a bond path motif of **1** and **2** is shown in Figure 2b,c (the bond path motif of $Ph_3PB(C_6F_5)_3$[24] is given in the SI). The common topological bond descriptors derived from analysis of the ED are collected in Table 2. In **1**, the short P−B distance gives rise to formation of a P−B bond critical point (bcp) with an ED value of 0.54 e $Å^{-3}$, which agrees well with the results for $Ph_3PB(C_6F_5)_3$ (0.57 e $Å^{-3}$) and a recent study on related phosphinonaphthylboranes **IIIc**−**IIIe** (Scheme 1).[9] In terms of bond topology, also

dx.doi.org/10.1021/ic401406k | *Inorg. Chem.* 2013, 52, 11881−11888

Table 1. Selected Interatomic Distances [Å] and Angles [deg] of 1 and 2

	1	2
Peri-Region Distances		
P1−B1	2.162(2)	3.050(3)
Peri-Region Bond Angles		
B1−C10−C19	119.1(2)	128.9(3)
C10−C19−C18	118.8(3)	127.1(2)
P1−C18−C19	110.8(2)	119.2(2)
∑ of bay angles	348.7(7)	375.2(7)
splay angle[a]	−11.3	15.2
C20−P1−C30	103.7(2)	113.2(4)
C40−B1−C50	118.5(2)	119.5(2)
Out-of-Plane Displacement		
P1	0.2753(5)	0.173(1)
B1	0.268(3)	0.369(3)
Central (Ace)Naphthyl Ring Torsion Angles		
C13−C14−C19−C18	174.9(3)	−175.2(7)
C15−C14−C19−C10	174.3(3)	−176.6(7)

[a]Splay angle: ∑ of the three bay region angles, −360°.

two weak H−P interactions are found that connect two methyl groups of the mesityl substituents with the P atom. Taking into account these two H atoms, the P atom is set in a distorted octahedral environment. According to all topological bond descriptors, the P−B, P−C, and B−C bonds are of polar-covalent nature:

The ED values are moderate, the corresponding Laplacian of the ED is negative but never below −10 e Å^{-5}, the kinetic energy density over ρ ratio $[G/\rho(r)_{bcp}]$ is significantly positive, and the potential energy density over ρ ratio $[V/\rho(r)_{bcp}]$ is negative, as expected for a covalent interaction. However, the H−P interactions are purely electrostatic, which is reflected in a positive Laplacian of the ED and a positive total energy over the density ratio $[H/\rho(r)_{bcp}]$.

The stability of this setting is reflected in the bond topology of the corresponding virial field of **1**, in which all bond critical points found in the ED are retained (see the SI). However, the situation is totally different for **2** because no P−B bond critical point is exhibited at all (Figure 2c). Instead, an extremely curved bond path is found connecting the P atom with the *ipso*-C atom of one mesityl ring; see the black arrow. The extreme curvature of the P−C(mesityl) bond path is a hint that this topological setting is close to a catastrophic scenario, which is supported by the virial field, which shows neither a P−B nor a P−C(mesityl) bond path (Figure 2d). Moreover, also one of the H−P bond critical points is extinguished in the virial field of **2**, confirming the nonbonding situation between the $BMes_2$ and PPh_2 fragments. The results of bond topology are supported by the curvedness mapped on the Hirshfeld surfaces of atomic fragments. This method uncovers contact patches between any type of fragments (atoms, functional groups, molecules, etc.), regardless of the strength or nature of the interaction. It is a fast and reliable tool for distinction of bonding from nonbonding contacts and can easily be calculated from X-ray structures. In Figure 3a,b, the curvedness is mapped on the Hirshfeld surface of the P atom in **1** and **2**, respectively. The corresponding results for $Ph_3PB(C_6F_5)_3$[24] are given in the SI. Consistent with topological analysis of the ED, only for **1** a significant

Table 2. Bond Topological Properties of 1, 2, and $Ph_3PB(C_6F_5)_3$[a]

	X−Y	d [Å]	$\rho(r)_{bcp}$ [e Å^{-3}]	$\Delta\rho(r)_{bcp}$ [e Å^{-5}]	d_1 [Å]	d_2 [Å]	ε	λ_3 [e Å^{-5}]	$G/\rho(r)_{bcp}$ [h e^{-1}]	$H/\rho(r)_{bcp}$ [h e^{-1}]
1	P1−B1	2.162	0.54	−1.9	1.408	0.754	0.22	1.39	0.34	−0.59
	P1−C18	1.810	1.15	−6.6	0.723	1.087	0.02	4.45	0.61	−1.01
	P1−C20	1.819	1.14	−7.9	0.744	1.075	0.14	3.06	0.50	−0.99
	P1−C30	1.829	1.12	−7.3	0.740	1.089	0.06	3.38	0.53	−0.99
	B1−C10	1.619	1.11	−4.1	0.530	1.089	0.11	9.90	0.77	−1.03
	B1−C40	1.652	1.06	−5.3	0.545	1.107	0.09	7.51	0.66	−1.01
	B1−C50	1.635	1.10	−5.7	0.540	1.094	0.11	8.04	0.67	−1.03
	P1−H46a	2.595	0.09	0.9	1.603	0.990	1.80	1.23	0.65	0.07
	P1−H58a	2.588	0.10	0.9	1.614	0.985	0.28	1.39	0.60	0.06
2	P1−C50[b]	3.050	0.11	0.7	1.680	1.440	2.33	1.09	0.47	0.00
	P1−C18	1.811	1.14	−6.1	0.724	1.088	0.07	4.51	0.63	−1.01
	P1−C20	1.920	0.96	−6.7	0.842	1.078	0.12	1.96	0.29	−0.78
	P1−C30	1.964	0.90	−5.3	0.906	1.058	0.09	2.54	0.25	−0.66
	B1−C10	1.585	1.20	−5.7	0.525	1.062	0.22	10.68	0.73	−1.07
	B1−C40	1.592	1.22	−7.5	0.533	1.059	0.21	8.96	0.64	−1.07
	B1−C50	1.585	1.23	−7.0	0.529	1.057	0.17	9.69	0.68	−1.08
	P1−H46a	2.852	0.07	0.6	1.787	1.065	0.09	0.92	0.52	0.07
	P1−H56a	2.939	0.06	0.6	1.866	1.066	0.13	0.89	0.54	0.08
$Ph_3PB(C_6F_5)_3$	P1−B20	2.181	0.57	−2.7	1.384	0.797	0.00	1.51	0.22	−0.56
	P1−C2	1.830	1.13	−8.7	0.765	1.065	0.10	2.09	0.42	−0.96
	P1−C7	1.819	1.15	−7.9	0.738	1.081	0.10	3.19	0.52	−1.00
	P1−C14	1.821	1.14	−8.3	0.748	1.073	0.10	2.92	0.48	−0.99
	B20−C21	1.634	1.05	−3.8	0.535	1.099	0.06	9.19	0.75	−1.01
	B20−C32	1.637	1.05	−3.9	0.536	1.101	0.05	9.06	0.75	−1.00
	B20−C43	1.639	1.05	−3.7	0.535	1.103	0.06	9.19	0.76	−1.00

[a]For all bonds, $\rho(r)_{bcp}$ is the ED at the bond critical point, $\Delta\rho(r)_{bcp}$ is the corresponding Laplacian, d_1 and d_2 are the distances from the atom to the bond critical point, ε is the bond ellipticity ($\lambda_1/\lambda_2 - 1$; $\lambda_{1/2}$ = curvature perpendicular to the bond path), λ_3 is the curvature along the bond path, and $G/\rho(r)_{bcp}$ and $H/\rho(r)_{bcp}$ are the kinetic and total energy density over $\rho(r)_{bcp}$ ratios. Results were obtained by analysis of the wavefunction files with *AIM2000*.[32]. [b]The P−C50 bond critical point is located close to the P−B axis.

dx.doi.org/10.1021/ic401406k | *Inorg. Chem.* 2013, 52, 11881−11888

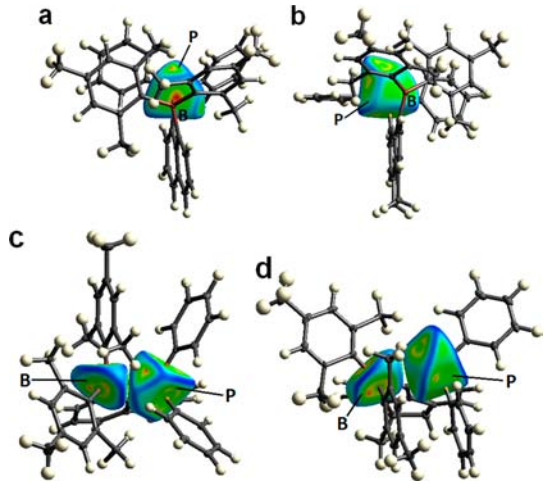

Figure 3. Curvedness mapped on the Hirshfeld surfaces of atomic fragments of the experimental X-ray structures of **1** and **2**. In parts a and b, the surfaces are given for the P atom, and in parts c and d, the surfaces are given for the P and B atoms. *CrystalExplorer* presentation.[37]

curvedness is found in the direction to the B atom (red color). If the Hirshfeld surfaces for the P and B atoms are displayed together [parts c (**1**) and d (**2**) of Figure 3], the atomic fragments are connected in the case of **1**, whereas the Hirshfeld surfaces of the P and B atoms are clearly separated from each other in **2** (Figure 3d). Accordingly, both parameters (curvedness as well as Hirshfeld surface fusion/separation) help to discriminate a bonding from a nonbonding scenario. Atomic fragments can also be generated from the three-dimensional ED following the topological approach of the AIM theory. The ED within these AIM atoms can be integrated, resulting in atomic properties such as charges, volumes, and atomic dipole moments.

By adding atomic charges according to functional groups in a molecular structure, charge separation and substituent effects become visible (in terms of AIM space partitioning). In this work, we analyze the following groups: The P atom, the two phenyl groups attached to the P atom, the B atom, the two mesityl groups attached to the B atom, and the (ace)naphthyl fragment. In both compounds, the (ace)naphthyl fragment carries an AIM charge of −1.12 e. Obviously, the P−B interaction has no significant effect on this part of the molecule.

The phenyl rings carry −0.46/−0.44 e in **1** [−0.37/−0.39/−0.39 e in $Ph_3PB(C_6F_5)_3$[24]] compared to −0.38/−0.29 e in **2**. The positively charged P atoms of **1** and **2**, however, show a remarkable difference of +0.45 e [+1.61 e in **1** and +1.60 e in $Ph_3PB(C_6F_5)_3$[24] compared to +1.16 e in **2**]. As for the phenyl rings, the effects on the dimesitylboron fragments are much smaller. The charges of the B atoms are +1.73 e in **1** [+1.73 e in $Ph_3PB(C_6F_5)_3$[24]] compared to +1.93 e in **2**, whereas the mesityl groups are almost equal (−0.67/−0.67 e in **1** compared to −0.67/−0.63 e in **2**). As a consequence, considering **2** as a nonbonding reference to **1**, it might be stated that the P−B fragment undergoes a partial charge compensation upon P−B bond formation (+0.12 e difference in **1** compared to the +0.87 e difference in **2**). A complementary view is provided by inspection of integrated electron populations within distinct bonding or lone-pair basins generated by space partitioning according to the ELI-D scheme. In agreement with the results of the topological AIM and Hirshfeld surface analysis, no disynaptic P−B valence basin [V_2(P,B)] is observed in **2**. Instead, an isolated lone-pair basin V_1(P) is found. Isosurface localization domain representations of the ELI-D for **1** and **2** are shown in Figure 4a,b. Representation of the P−B bonding

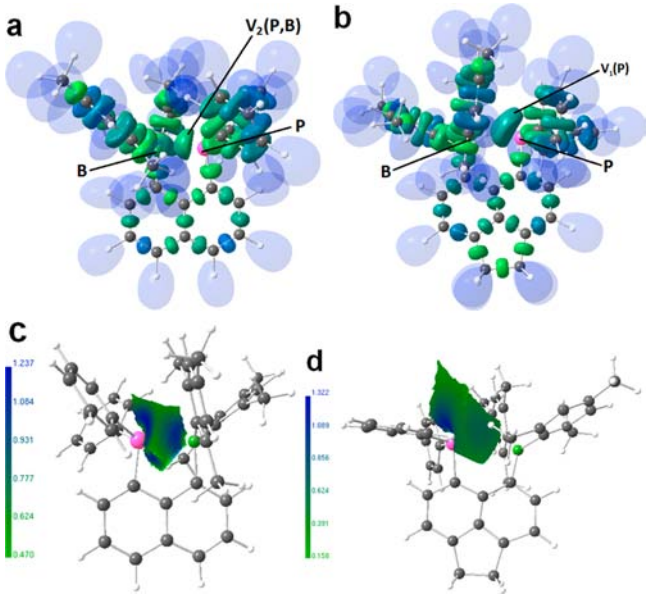

Figure 4. (a and b) Isosurface representations of the ELI-D localization domains (Y = 1.4) of **1** and **2**. The surfaces are color-coded according to the basin size transforming from green (small) to blue (large). For clarity, protonated valence basins (H atoms) are given in transparent mode. (c and d) ELI-D mapped on the basin surfaces of V_2(P,B) in **1** and V_1(P) in **2**. P atoms are pink, and B atoms are green. *MOLISO* presentation.[39]

basin of **1** and the lone-pair basin of the P atom in **2** are displayed in Figure 4c,d. The corresponding results for $Ph_3PB(C_6F_5)_3$[24] are given in the SI. A comparison of parts a and b of Figure 4 reveals that V_2(P,B) in **1** is smaller than V_1(P) in **2** and that V_2(P,B) is located between the P and B atoms. When the ELI-D is mapped on the basin surfaces, distinct effects of the electron localizability become visible. This method was first utilized in a recent analysis of atom−atom connectivities in zincocenes and helps to discriminate bonding from nonbonding scenarios.[38] A comparison of parts c and d of Figure 4 reveals that in **1** a ring-shaped region of increased electron localizability is located at the side pointing toward the B atom. However, such a kind of ELI-D distribution is not found on the corresponding side of the V_1(P) basin in **2**.

For the zincocenes, the outer-core basin of the Zn atoms comprising 3s, 3p, and 3d electrons was analyzed and showed clear distortions in the shape and typical distributions of the ELI-D on the core basin surfaces according to the bonding scenario.[38] In this work, we analyzed the outer-core basin of the P atom, which comprises the 2s and 2p electrons, but in contrast to the outer-core basin in the zincocenes, neither in shape nor in ELI-D distribution, this basin is affected by the appearance or absence of a P−B bond (see the SI). The qualitative results are supported by the quantitative ELI-D-derived bond descriptors listed in Table 3. The lone-pair basin of the P atom carries +2.11 e in a basin of 12.7 Å^3. As the RJI shows, this density is to 98% located in the AIM P atom. However, only 0.2% of the remaining 2% are located inside the AIM B atom. The majority is distributed over several adjacent

dx.doi.org/10.1021/ic401406k | *Inorg. Chem.* 2013, 52, 11881−11888

Table 3. Topological and Integrated ELI-D Properties of 1, 2, and $Ph_3PB(C_6F_5)_3$[a]

	basin	$V(001)_{ELI}$ [Å^3]	$N(001)_{ELI}$ [e]	Y_{max}	d_{ELI} [Å]	RJI [%]
1	V_2(P1,B1)	6.9	1.97	2.05	0.291	86
	V_2(P1,C18)	5.3	2.23	1.91	0.083	76
	V_2(P1,C20)	5.3	2.22	1.91	0.006	75
	V_2(P1,C30)	5.0	2.19	1.91	0.032	75
	V_2(B1,C10)	5.0	2.21	2.10	0.018	87
	V_2(B1,C40)	5.5	2.23	2.08	0.050	85
	V_2(B1,C50)	5.6	2.25	2.10	0.027	85
2	V_1(P1)	12.7	2.11	2.40	0.309	98[b]
	V_2(P1,C18)	4.6	2.10	1.87	0.050	77
	V_2(P1,C20)	5.2	2.08	1.87	0.078	72
	V_2(P1,C30)	5.3	2.04	1.83	0.091	69
	V_2(B1,C10)	6.3	2.38	2.11	0.101	86
	V_2(B1,C40)	5.8	2.27	2.13	0.008	85
	V_2(B1,C50)	6.2	2.37	2.10	0.029	85
Ph_3P $B(C_6F_5)_3$	V_2(P1,B20)	7.2	1.95	2.10	0.001	81
	V_2(P1,C2)	5.3	2.20	1.91	0.017	73
	V_2(P1,C7)	5.2	2.21	1.91	0.022	74
	V_2(P1,C14)	5.2	2.20	1.91	0.006	74
	V_2(B20,C21)	5.6	2.22	2.07	0.009	87
	V_2(B20,C32)	5.7	2.22	2.07	0.019	87
	V_2(B20,C43)	5.7	2.22	2.08	0.013	87

[a] $V_2(X,Y)$ are disynaptic valence (bonding) basins, $V_1(X)$ is a (nonbonding) lone-pair basin. For all basins, $V(001)_{ELI}$ is the basin volume cut at 0.001 au, $N(001)_{ELI}$ is the corresponding electron population in that volume, Y_{max} is the ELI-D value at the attractor position, d_{ELI} is the perpendicular distance of the attractor position to the atom−atom line, RJI is the Raub−Jansen index (percental electron population within the AIM atom that has the larger electronegativity). Results were obtained by analysis of grid files using *DGRID-4.5*.[33] The grid step size is 0.05 bohr. [b] Only 0.18% are located within the AIM B atom.

AIM atoms, which clearly contradicts a dative P−B bond and is simply due to the different space-partitionings in AIM and ELI-D, respectively. This very small overlap between the AIM and ELI-D basins uncovers that the corresponding zero-flux surfaces are almost equal in shape and position in **2**, thus supporting the nonbonding situation. The P−B bonding basin in **1** carries +1.97 e in a volume of 6.9 Å^3 [in $Ph_3PB(C_6F_5)_3$,[24] +1.95 e in 7.2 Å^3], which is a considerable reduction compared to the values for the V_1(P) basin in **2**. In contrast to the dative N−B interaction in Lewis acid−base adducts or *archno*-boranes,[23] the P−B contact is obviously of polar-covalent nature like all listed P−C and B−C bonds, which is reflected in RJI values significantly below 90%. This is in sharp contrast to the dative bond description used by Wang et al. for **1**.[6] Because of the sterical restrictions imposed by the aromatic group, also in **1**, the P−B interactions remain strained. This is visible in the geometrical distortions of the molecular structure, as mentioned above, and in the quite large distance of the ELI-D attractor position to the P−B axis [d_{ELI} = 0.291 Å compared to 0.001 Å in $Ph_3PB(C_6F_5)_3$], which is almost identical with the value for the V_1(P) basin in **2** (d_{ELI} = 0.309 Å).

CONCLUSIONS

1 and **2** containing the same substituents in the *peri* positions, namely, diphenylphosphino and dimesitylboron groups, have been prepared and fully characterized. Despite their structural similarities, **1** and **2** possess quite different P−B *peri* distances of 2.162(2) and 3.050(3) Å, respectively, which classifies them as straightforward cases of regular Lewis pairs and FLPs. Analysis of a set of RSBIs derived from the theoretically calculated electron and pair densities confirms the bonding and nonbonding states of the P and B atoms. In a complementary study, Bourissou et al.[9] demonstrated that fine-tuning of bonding P−B *peri* distances is possible by variation of the substituents attached at the B atoms in **IIIc**−**IIIe** showing *peri* P−B distances of 2.173(4), 2.076(2), and 2.011(2) Å, respectively. Taking into account also the very recent study of Tokitoh et al.,[7,8] a series of three 1-disubstituted phosphino-8-naphthyl-dimesitylboranes, **1**, **IIIb**, and **IIIc**, containing different substituents attached to the P atoms is now available. Because the substituents (Ph, *i*-Pr, and Cl) are approximately the same size, the different *peri* P−B distances of 2.162(2), 2.892(2), and 2.173(4) Å are obviously due to electronic effects.

ASSOCIATED CONTENT

Supporting Information

X-ray crystallographic data in CIF format, crystal data and structure refinement of **1** and **2**, NMR spectra of **1** and **2**, and additional information on analysis of the real-space bond descriptors of **1** and **2**. This material is available free of charge via the Internet at http://pubs.acs.org.

AUTHOR INFORMATION

Corresponding Authors

*E-mail: j.beckmann@uni-bremen.de.
*E-mail: stebs@chemie.fu-berlin.de.

Notes

The authors declare no competing financial interest.

ACKNOWLEDGMENTS

Deutsche Forschungsgemeinschaft (DFG) is gratefully acknowledged for financial support. Prof. Dr. T. Sasamori is kindly thanked for making available to us a copy of his oral presentation.[8]

DEDICATION

Dedicated to Prof. Dainis Dakternieks on the occasion of his 65th birthday.

REFERENCES

(1) Stephan, D. W.; Erker, G. *Angew. Chem.* **2010**, *122*, 50−81; *Angew. Chem., Int. Ed.* **2010**, *49*, 46−76.
(2) Erker, G. *Dalton Trans.* **2011**, *40*, 7475−7483.
(3) Stephan, D. W. *Org. Biomol. Chem.* **2012**, *10*, 5740−5746.
(4) Wang, H.; Fröhlich, R.; Kehr, G.; Erker, G. *Chem. Commun.* **2008**, 5966−5968.
(5) Jiang, C.; Blacque, O.; Berke, H. *Chem. Commun.* **2009**, 5518−5520.
(6) Li, Y.-F.; Kang, Y.; Ko, S.-B.; Rao, Y.; Sauriol, F.; Wang, S. *Organometallics* **2013**, *32*, 3063−3068.
(7) Tsurusaki, S.; Sasamori, T.; Wakamiya, A.; Yamaguchi, S.; Nagura, K.; Irle, S.; Tokitoh, N. *Angew. Chem.* **2011**, *123*, 11132−11135; *Angew. Chem., Int. Ed.* **2011**, *50*, 10940−10943.
(8) Sasamori, T.; Tsurusaki, A.; Tokitoh, N.; Wakamiya, A.; Nagura, K.; Irle, S.; Yamaguchi, S. *Oral presentation No. O21, 13th International Symposium of Inorganic Ring Systems (IRIS 13)*, Victoria, British Columbia, Canada, 2012; 29.7-2.8.
(9) Bontemps, S.; Devillard, M.; Mallet-Ladeira, S.; Bouhadir, G.; Miqueu, K.; Bourissou, D. *Inorg. Chem.* **2013**, *52*, 4714−4720.
(10) Wade, C. R.; Saber, M. R.; Gabbaï, F. P. *Heteroatom Chem.* **2011**, *22*, 500−505.
(11) Gabbaï, F. P.; Zhao, H. *Nat. Chem.* **2010**, 984−990.
(12) Wade, C. R.; Gabbaï, F. P. *Organometallics* **2011**, *30*, 4479−4481.
(13) Zhao, H.; Gabbaï, F. P. *Org. Lett.* **2011**, *13*, 1444−1446.
(14) Aschenbach, L. K.; Knight, F. R.; Randall, R. A. M.; Cordes, D. B.; Baggott, A.; Bühl, M.; Slawin, A. M. Z.; Woollins, J. D. *Dalton Trans.* **2012**, *41*, 3141−3153.
(15) Lin, T.-P.; Wade, C. R.; Pérez, L. M.; Gabbaï, F. P. *Angew. Chem.* **2010**, *122*, 6501−6504; *Angew. Chem., Int. Ed.* **2010**, *49*, 6357−6360.
(16) Zhao, H.; Gabbaï, F. P. *Organometallics* **2011**, *31*, 2327−2335.
(17) (a) Mallinson, P. R.; Woźniak, K.; Smith, G. T.; McGormack, K. L. *J. Am. Chem. Soc.* **1997**, *119*, 11502−11509. (b) Mallinson, P. R.; Woźniak, K.; Wilson, Ch. C.; McGormack, K. L.; Yufit, D. S. *J. Am. Chem. Soc.* **1999**, *121*, 4640−4646. (c) Hoser, A. A.; Dobrzycki, Ł.; Gutmann, M. J.; Woźniak, K. *Cryst. Growth Des.* **2010**, *10*, 5092−5104.
(18) (a) Bader, R. F. W. *Atoms in Molecules: A Quantum Theory*; Cambridge University Press: Oxford U.K., 1991. (b) Gatti, C. *Z. Kristallogr.* **2005**, 399−457.
(19) Hirshfeld, F. L. *Theor. Chim. Acta* **1977**, *44*, 129−139.
(20) Kohout, M. *Int. J. Quantum Chem.* **2004**, *97*, 651−658.
(21) Spackman, M. A.; Byrom, P. G. *Chem. Phys. Lett.* **1997**, *267*, 215−220.
(22) (a) Raub, S.; Jansen, G. *Theor. Chem. Acc.* **2001**, *106*, 223−232. (b) Vidal, I.; Melchor, S.; Dobado, J. A. *J. Phys. Chem. A* **2005**, *109*, 7500−7508.
(23) (a) Mebs, S.; Grabowsky, S.; Förster, D.; Kickbusch, R.; Hartl, M.; Daemen, L. L.; Morgenroth, W.; Luger, P.; Paulus, B.; Lentz, D. *J. Phys. Chem. A* **2010**, *114*, 10185−10196. (b) Mebs, S.; Kalinowski, R.; Grabowsky, S.; Förster, D.; Kickbusch, R.; Justus, E.; Morgenroth, W.; Paulmann, C.; Luger, P.; Gabel, D.; Lentz, D. *J. Phys. Chem. A* **2011**, *115*, 1385−1395.
(24) Jacobsen, H.; Berke, H.; Döring, S.; Kehr, G.; Erker, G.; Fröhlich, R.; Meyer, O. *Organometallics* **1999**, *18*, 1724−1735.
(25) Beckmann, J.; Do, T. G.; Grabowsky, S.; Hupf, E.; Lork, E.; Mebs, S. *Z. Anorg. Allg. Chem.* **2013**, DOI: 10.1002/zaac.201300272.
(26) Eisch, J. J.; Shafii, B.; Odom, J. D.; Rheingold, A. L. *J. Am. Chem. Soc.* **1990**, *112*, 1847−1853.
(27) Dolomanov, O. V.; Bourhis, L. J.; Gildea, R. J.; Howard, J. A. K.; Puschmann, H. *J. Appl. Crystallogr.* **2009**, *42*, 339−341.
(28) (a) Perdew, J. P.; Chevary, J. A.; Vosko, S. H.; Jackson, K. A.; Pederson, M. R.; Singh, D. J.; Fiolhais, C. *Phys. Rev. B* **1992**, *46*, 6671−6687. (b) Becke, A. D. *J. Chem. Phys.* **1993**, *98*, 5648−5652.
(29) (a) Peterson, K. A.; Figgen, D.; Goll, E.; Stoll, H.; Dolg, M. *J. Chem. Phys.* **2003**, *119*, 11113−11123. (b) Metz, B.; Stoll, H.; Dolg, M. *J. Chem. Phys.* **2000**, *113*, 2563−2569. (c) Peterson, K. A. *J. Chem. Phys.* **2003**, *119*, 11099−11112.
(30) Frisch, M. J.; Trucks, G. W.; Schlegel, H. B.; Scuseria, G. E.; Robb, M. A.; Cheeseman, J. R.; Scalmani, G.; Barone, V.; Mennucci, B.; Petersson, G. A.; Nakatsuji, H.; Caricato, M.; Li, X.; Hratchian, H. P.; Izmaylov, A. F.; Bloino, J.; Zheng, G.; Sonnenberg, J. L.; Hada, M.; Ehara, M.; Toyota, K.; Fukuda, R.; Hasegawa, J.; Ishida, M.; Nakajima, T.; Honda, Y.; Kitao, O.; Nakai, H.; Vreven, T.; Montgomery, J. A., Jr.; Peralta, J. E.; Ogliaro, F.; Bearpark, M.; Heyd, J. J.; Brothers, E.; Kudin, K. N.; Staroverov, V. N.; Kobayashi, R.; Normand, J.; Raghavachari, K.; Rendell, A.; Burant, J. C.; Iyengar, S. S.; Tomasi, J.; Cossi, M.; Rega, N.; Millam, J. M.; Klene, M.; Knox, J. E.; Cross, J. B.; Bakken, V.; Adamo, C.; Jaramillo, J.; Gomperts, R.; Stratmann, R. E.; Yazyev, O.; Austin, A. J.; Cammi, R.; Pomelli, C.; Ochterski, J. W.; Martin, R. L.; Morokuma, K.; Zakrzewski, V. G.; Voth, G. A.; Salvador, P.; Dannenberg, J. J.; Dapprich, S.; Daniels, A. D.; Farkas, Ö.; Foresman, J. B.; Ortiz, J. V.; Cioslowski, J.; Fox, D. J. *Gaussian09*, revision B.01; Gaussian, Inc.: Wallingford, CT, 2009.
(31) Wilson, A. J. C. *International Tables of Crystallography*; Kluwer Academic Publishers: Boston, 1992; Vol. *C*.
(32) Biegler-König, F.; Schönbohm, J.; Bayles, D. *J. Comput. Chem.* **2001**, *22*, 545−559.
(33) Kohout, M. *DGrid*, version 4.5; Radebeul, Germany, 2009.
(34) Brandenburg, K. *DIAMOND*, version 3.2i; Crystal Impact GbR: Bonn, Germany, 2012.
(35) Bondi, A. *J. Phys. Chem.* **1964**, *68*, 441−451.
(36) Keller, E. *SCHAKAL*; Albert Ludwigs Universität: Freiburg, Germany, 1999.
(37) Wolff, S. K.; Grimwood, D. J.; McKinnon, J. J.; Turner, M. J.; Jayatilaka, D.; Spackman, M. A. *CrystalExplorer*, version 3.0; University of Western Australia, Crawley, Australia, 2012.
(38) Mebs, S.; Chilleck, M.; Grabowsky, S.; Braun, T. *Chem.—Eur. J.* **2012**, *18*, 11647−11661.
(39) Hübschle, C. B.; Luger, P. *J. Appl. Crystallogr.* **2006**, *39*, 901−904.